SCIENTIFIC REPORTS

OPEN

SUBJECT AREAS:
STRUCTURAL PROPERTIES
SENSORS

Received
15 August 2014

Accepted
15 December 2014

Published
19 January 2015

Correspondence and requests for materials should be addressed to B.C. (mse_caobq@ujn.edu.cn) or X.X. (sps_xuxj@ujn.edu.cn, phys_xu@hotmail.com)

Morphology-modulation of SnO_2 Hierarchical Architectures by Zn Doping for Glycol Gas Sensing and Photocatalytic Applications

Qinqin Zhao[1], Dianxing Ju[2], Xiaolong Deng[1], Jinzhao Huang[1], Bingqiang Cao[2] & Xijin Xu[1]

[1]School of Physics and Technology, University of Jinan, 336 West Road of Nan Xinzhuang, Jinan, 250022, Shandong Province, Peoples Republic of China, [2]School of Materials Science and Engineering, University of Jinan.

The morphology of SnO_2 nanospheres was transformed into ultrathin nanosheets assembled architectures after Zn doping by one-step hydrothermal route. The as-prepared samples were characterized in detail by various analytical techniques including scanning electron microscopy (SEM), transmission electron microscopy (TEM), X-ray diffraction (XRD), and nitrogen adsorption-desorption technique. The Zn-doped SnO_2 nanostructures proved to be the efficient gas sensing materials for a series of flammable and explosive gases detection, and photocatalysts for the degradation of methyl orange (MO) under UV irradiation. It was observed that both of the undoped and Zn-doped SnO_2 after calcination exhibited tremendous gas sensing performance toward glycol. The response ($S = R_a/R_g$) of Zn-doped SnO_2 can reach to 90 when the glycol concentration is 100 ppm, which is about 2 times and 3 times higher than that of undoped SnO_2 sensor with and without calcinations, respectively. The result of photocatalytic activities demonstrated that MO dye was almost completely degraded (~92%) by Zn-doped SnO_2 in 150 min, which is higher than that of others (MO without photocatalyst was 23%, undoped SnO_2 without and with calcination were 55% and 75%, respectively).

As one of the most important classes of materials, metal oxide semiconductors are presenting themselves in various areas of science and technology, due to their desirable morphologies and distinct structures[1,2]. SnO_2, a typical n-type semiconductor with a wide band gap (3.6 ev)[3–5], has been widely investigated with many applications such as gas sensors[6–9], solar cells[10], lithium batteries[11], catalysis[12–15], and transparent conductive electrodes[16], because of its unique optical, catalytic, and electrical properties and high chemical stability. It has been reported that the performances of SnO_2 nanomaterials are greatly affected by their morphology, structure and surface area[17]. Therefore, it is believed that their advanced nanostructured materials with different dimensionalities would offer good opportunities to explore new physical and chemical applications including gas sensors and photocatalysis. Recently, Guo et al.[18]. reported that the sensor, fabricated by 3D SnO_2 microstructures assembled by porous nanosheets through hydrothermal synthesis, exhibited good response-recovery performance, high sensitivity and excellent long-term stability for ethanol gas. Dai et al. synthesized flower-like SnO_2 microstructures which exhibited higher photoactivity (about 2.2 times) than granular SnO_2 for the degradation of RhB dye[19]. These structural features can improve both the sensing performance and the photocatalytic degradation rate. In this view, the more attention should be paid to the design and synthesis of hierarchical SnO_2 nanomaterials.

In order to satisfy the increasing demands for the photocatalysts or gas sensors working under harsh and complicated conditions, many efforts have been made to improve the performance of SnO_2 materials such as doping[20–23], adding catalysts[24–26], and constructing the heterojunctions[27,28]. Among these methods, doping has been proposed to be a facile efficient way to modulate their properties. In particular, the previous reports demonstrated that the morphologies and properties of SnO_2 could be modified by Zn doping[29–32]. This could be attributed to the facile substitution of Sn ions by Zn ions due to the similar ion radius of Zn^{2+} and Sn^{4+} (Zn^{2+} 0.074 nm, Sn^{4+} 0.071 nm), which may produce more oxygen vacancies for charge compensation and further enhance the performance of SnO_2. Thus, it is expected that Zn-doped SnO_2 hierarchical nanostructures will provide excellent gas sensing and photocatalytic properties.

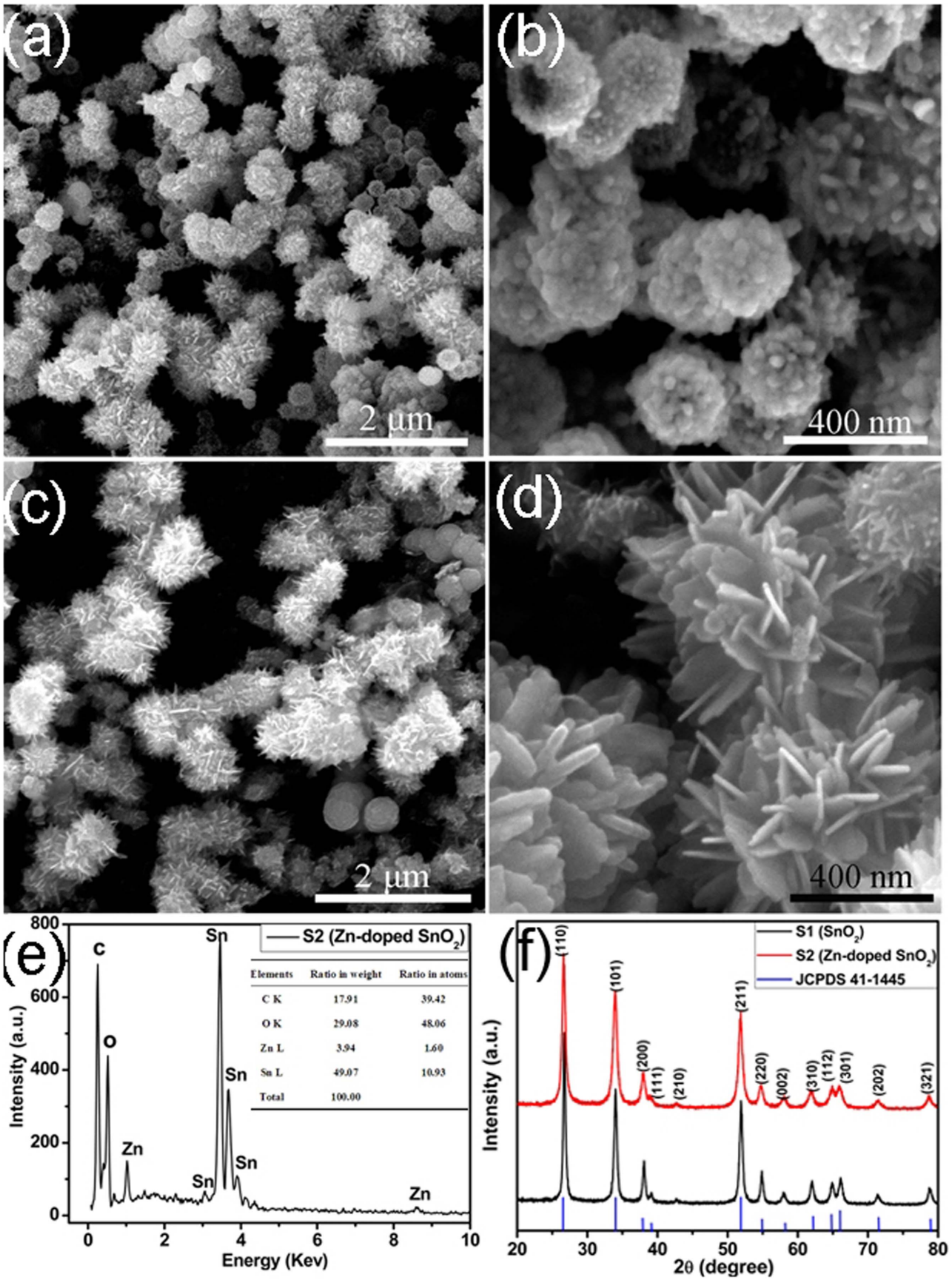

Figure 1 | SEM images of undoped (a, b) and Zn-doped SnO_2 (c, d). (e) EDS spectra of Zn-doped SnO_2 shown in (c, d). (f) XRD patterns of undoped and Zn-doped SnO_2. Undoped (S1 600°C) and Zn-doped SnO_2 (S2 600°C).

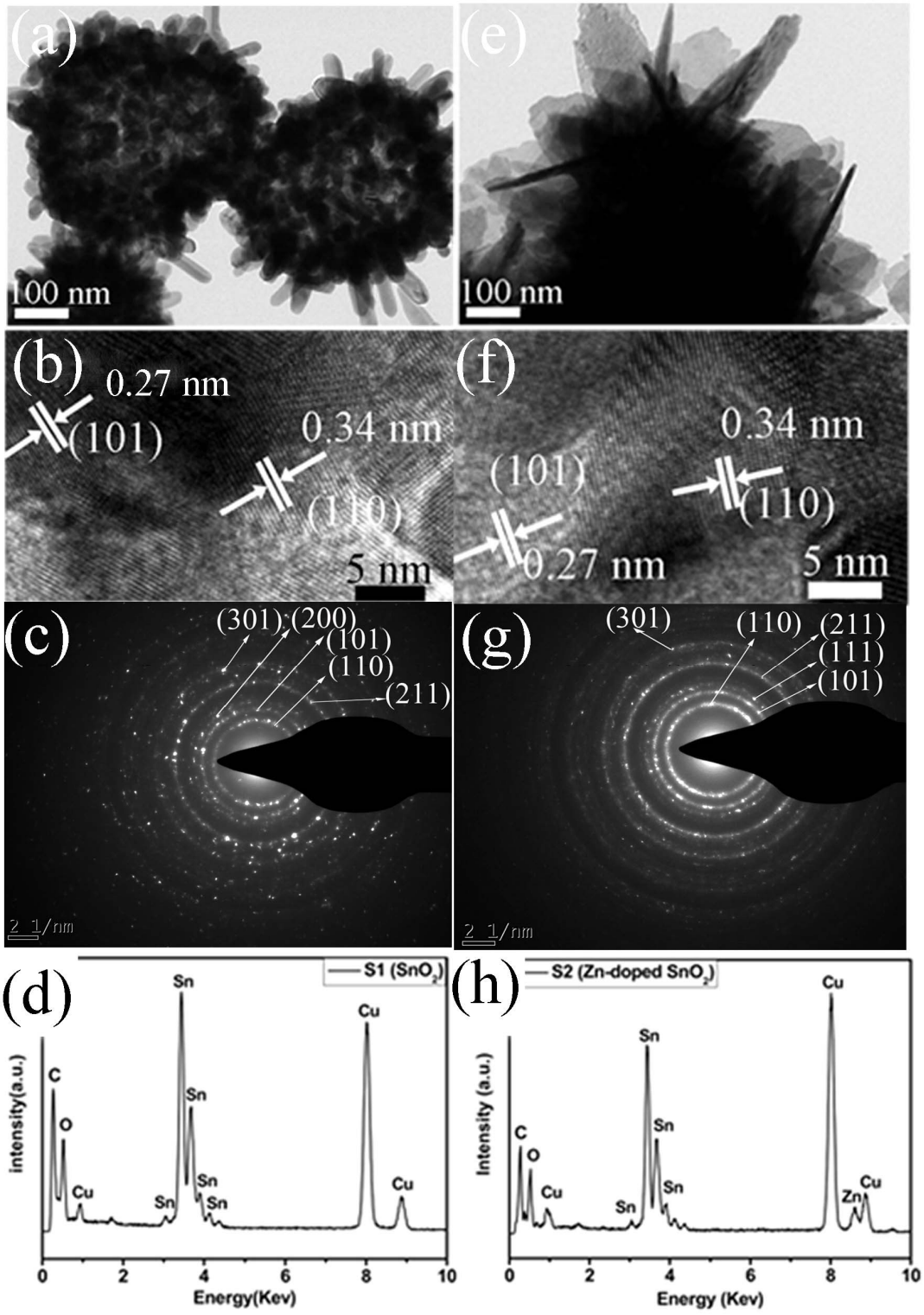

Figure 2 | (a) and (e) TEM images of undoped and Zn-doped SnO_2; (b, f) HRTEM images of undoped and Zn-doped SnO_2 with their SAED pattern (c, g)); (d, h) EDX spectra of undoped and Zn-doped SnO_2. Undoped (S1 600°C) and Zn-doped SnO_2 (S2 600°C). The peaks of Cu and C observed in the EDX spectrum are from carbon-coated copper grids.

Here, the Zn-doped SnO_2 hierarchical nanostructures were synthesized by one-step hydrothermal process, which are composed of a number of nanosheets with the thickness of about 30 nm. The as-prepared samples were applied to the glycol detection and the photocatalytic degradation of methyl orange (MO) under UV irradiation. The results indicated that Zn-doped SnO_2 hierarchical nanostructures had better glycol gas response and photocatalytic activity than undoped SnO_2 nanostructures.

Methods

Synthesis of undoped and Zn-doped SnO_2 hierarchical nanostructures. All chemicals were of analytical grade regents and used without any further purification. A typical synthesis process was as follows: 6 mM of NH_4F was dissolved in 50 ml of deionized water under vigorous magnetic stirring, followed by adding 2 mM of $SnCl_2 \cdot 2H_2O$ and 2 mM of $ZnCl_2$ into the above solution with the assistance of ultrasonication. The mixed solution was then transferred into a 100 ml Teflon-lined stainless steel autoclave, and kept at 180°C for 16 h in order to obtain the precipitates.

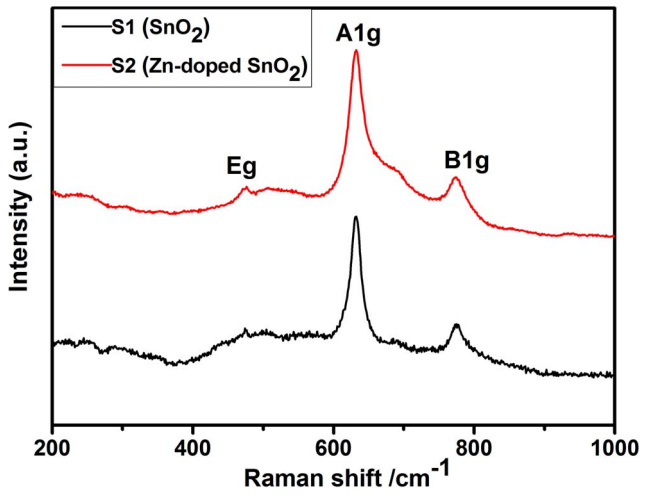

Figure 3 | Raman spectrum of undoped (S1 600°C) and Zn-doped SnO_2 (S2 600°C).

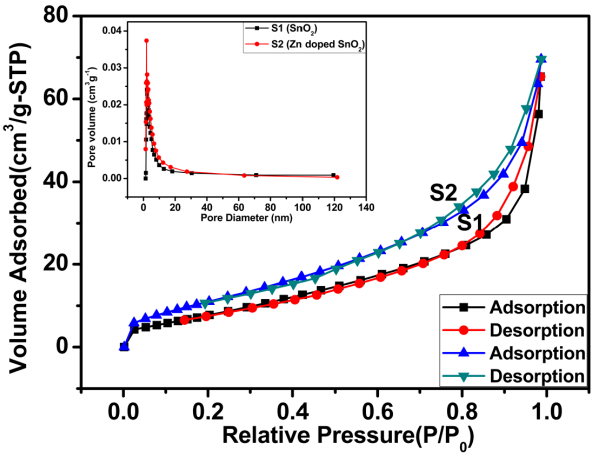

Figure 4 | Nitrogen adsorption-desorption isotherms and pore size distribution curves (inset) of S1 (SnO_2 600°C) and S2 (Zn-doped SnO_2 600°C).

Then, the autoclave cooled to room temperature naturally. The obtained products were collected and washed with deionized water and ethanol several times, respectively, and then dried in air at 60°C for 12 h. Finally, the products were annealed at 600°C for 2 h, named as S2. The undoped SnO_2 was obtained by the same process except the addition of $ZnCl_2$, named as S1. The undoped SnO_2 sample without calcination was named as S0.

Material Characterizations. The compositions and morphologies of the as-prepared samples were characterized by a field emission scanning electron microscope (FESEM, FEI QUANTA FEG250) equipped with an energy dispersive x-ray spectroscopy (EDS, INCA MAX-50) and a high-resolution transmission electron microscope (Tecnai G2 F20). The crystal structures of the samples were analyzed by X-ray diffraction (XRD, D8-Advance, Bruker) with Cu K_α radiation and Raman spectrometer (Renishaw inVia) in the range from 200 cm^{-1} to 1000 cm^{-1} at room temperature. The average pore size, pore volume, and specific surface area of the samples were examined through measuring N_2 adsorption-desorption isotherm with a Micromeritics ASAP2020 apparatus.

Fabrication and Gas-Sensing measurements. Gas sensors were fabricated as follows: The as-prepared sample was mixed with the deionized water to form a paste, and then it was coated onto an Al_2O_3 tube by a small brush to form a thick film between two parallel Au electrodes, which had been previously printed on the tube. A heater of Ni-Cr coil was inserted into the Al_2O_3 tube to keep the sensor at the operating temperature. The gas sensor properties were measured by a gas sensing test system (WS-30A, Weisheng Electronics, Zhengzhou, China) with a test voltage of 5 V under laboratory conditions (30% ± 10% RH, 23 ± 1°C). The devices were put into an airproof test box and tested by a static process in a test chamber. A given amount of the target gas was injected into the test chamber, when the response reached a constant value, the upper cover of the test chamber was removed and the sensor began to recover in air. The response of the sensor was defined as $S = R_a/R_g$ for target gas, where R_a and R_g are the sensor resistance in air and in target gas, respectively.

Photocatalytic Measurements. The photocatalytic activity of the samples was investigated by measuring the degradation of methyl orange (MO) under UV light (generated by a 500 W high pressure mercury lamp). Typically, 30 mg of as-prepared sample was added to the aqueous solution of MO dye (50 ml, 20 mg/L) with stirring in the dark for 30 min to ensure the absorption/desorption equilibrium. Then, the suspension was exposed to UV light irradiation whilst stirring. At given irradiation time intervals, concentrations of MO were monitored with a TU-1901 UV-vis spectrophotometer by measuring the absorbance at 464 nm during the degradation process.

Results and discussion

Representative morphologies and structures of the as-obtained SnO_2 nanostructures, revealed by field-emission scanning electron microscopy (SEM), are shown in Figure 1. The surface morphologies of undoped SnO_2 (S1) are shown in Figure 1(a, b). It can be seen that the products are mostly spherical-like structures with a relatively rough surface, which is consisted of SnO_2 nanorods. The morphologies of the Zn-doped SnO_2 (S2) are shown in Figure 1(c, d). Compared with the undoped sample, the products are composed of SnO_2 nanosheets, which may be attributed to the induced growth of Zn^{2+} ions, as shown in Figure 1(e). The peak of Zn can be clearly observed in the spectrum and the content ratio of Zn and Sn is about 1.60 : 10.93, shown in the insert table. Figure 1(f) shows the typical XRD patterns of the as-prepared undoped (S1) and Zn-doped SnO_2 (S2) architectures. All the diffraction peaks could be well indexed to the tetragonal rutile structure of SnO_2, which was consistent with the standard data file (JCPDS file no. 41–1445). No obvious characteristic peaks are observed for the impurities. Additionally, the diffraction peaks of the Zn-doped SnO_2 tend to become slightly broader from Figure 1(f), which could be attributed to the size effect of the crystals. The mean grain size of undoped and the Zn-doped SnO_2 were calculated to be 29.3 nm and 22.6 nm, respectively, using the Debye-Scherer formula, $D = 0.89\lambda/(\beta \cos\theta)$[33], where λ is the X-ray wavelength, θ is the Bragg diffraction angle and β is the peak full-width at half maximum.

The morphologies and microstructures of the samples S1 (SnO_2) and S2 (Zn-doped SnO_2) were further studied by TEM, as shown in Figure 2. From Figure 2(a), we get to know that the undoped SnO_2 (S1) is mainly comprised of spherical-like structures constructed by nanorods with a diameter of 20–30 nm and a length up to one hundred nanometers. This is in consistent with the SEM images in Figure 1(a, b). The HRTEM image is shown in Figure 2(b), in which the interplanar distances are 0.34 nm and 0.27 nm, respectively, matching well with (110) and (101) planes of rutile SnO_2. The selected area electron diffraction (SAED) pattern taken from the corresponding microspheres suggests a polycrystalline structure of as-prepared sample, as shown in Figure 2(c). The peak of Sn and O can be clearly observed in the spectrum from EDX spectrum (Figure 2(d)) for the undoped SnO_2 revealing a purity phase. The peaks of Cu and C observed in the spectrum are attributed to the carbon-coated copper grids.

Compared with the undoped SnO_2, the Zn-doped SnO_2 are mainly composed of SnO_2 nanosheets, as shown in Figure 2(e). The HRTEM image (Figure 2(f)) shows that the lattice fringes of the Zn-doped SnO_2 nanostuctures are 0.34 and 0.27 nm, which correspond to the (110) and (101) lattice planes of SnO_2, respectively, as shown in Figure 2(g). The SAED pattern indicates that the nanosheet is of polycrystalline structure composed of nanoscaled particles. Figure 2(h) shows the EDX spectrum of the Zn-doped SnO_2, in which the peak of Zn can be clearly observed in the spectrum, which is corresponding to the XRD pattern of Zn-doped SnO_2. Furthermore, it can be seen from the SEM and TEM images that SnO_2 nanorods change into nanosheets after the doping of Zn element. This evolution is ascribed to the successfully substitutional doping of Zn^{2+} ions into SnO_2 lattice with modification of local

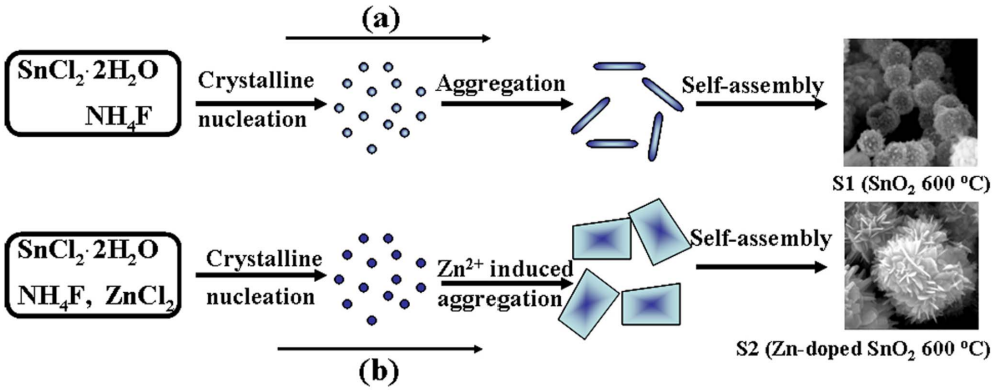

Figure 5 | **Schematic formation mechanisms of undoped (S1 600°C) and Zn-doped SnO_2 (S2 600°C).**

structure[34]. It is presumed that the modification of local structure varies the surface energy of some crystallographic planes in the prepared nanosheets, which changes the growth rate of these crystallographic planes. As can be seen in our experiment, Zn^{2+} ions in SnO_2 lattice inhibit the growth along [110] direction but permit the growth along the axis of nanorod, promoting the anisotropic growth of the nanorods[34]. Therefore, it is believed that Zn^{2+} serves as a structure-directing agent in the growth of nanosheets.

Raman scattering is generally used to investigate the crystallinity, structural defects, and size effects of nanoscale crystallites[35,36]. Figure 3 presents the room temperature Raman spectra of pure SnO_2 (S1) and Zn-doped SnO_2 (S2) architectures. The peaks at 630 and 774 cm^{-1} correspond respectively to A1g and B2g modes, which are related to the symmetric and asymmetric stretching of Sn-O bonds, respectively[36,37]. The peak at 475 cm^{-1} represents Eg doubly degenerate mode, arising from the vibration mode of oxide ions. The appearance of these "classical modes" confirms the tetragonal rutile structure of $Sn_{1-x}Zn_xO_2$ nanostuctures[37]. Compared with undoped SnO_2, the peaks located at 630 and 774 cm^{-1} of the Zn-doped SnO_2 Raman spectrum become broadened, which might be ascribed to the effects of oxygen deficiency and crystal distortion, caused by the introduction of Zn ions[36,38]. In addition, such broadening of A1g mode is referred to the decrease of grain size, which is consistent with the XRD results[39].

In order to further confirm the inner architectures, nitrogen adsorption and desorption measurements of the as-prepared products (S1 and S2) were carried out to estimate the properties, as shown in Figure 4. The specific surface area of the samples was calculated to be 51.2 and 61.8 m^2g^{-1}, respectively, indicating an uptrend of the active surface after the doping of Zn. Pore size distribution curves (inset of Figure 4) are important factors for mass transport and effective surface area. The average pore size of the two samples (S1 and S2) was calculated to be 8.798 nm and 7.676 nm, respectively. The pores distributed are also observed in TEM image (Figure 2(a, e)) between the adjacent nanoparticles. It clearly indicates that the Zn-doped SnO_2 shows a higher specific surface area than that of undoped SnO_2, which might be advantageous for enhancing gas sensing performance.

Some papers have reported that Zn-doped SnO_2 would form the nanorods or nanoneedles in the ethanol-water solution using KOH or NaOH as the alkali source[30,34]. This morphology may be attributed to the regulating function of Zn and alcohol which has been mentioned by many papers[29,39,40]. However, when the ethanol-water solution and alkali source were replaced by water and NH_4F solution as used in our case, the morphology of the products may be changed. According to the previous reports, a possible formation mechanism is proposed, as illustrated in Figure 5[34,41]. The tin precursor under a high temperature can be fast hydrolyzed to form $Sn(OH)_2$, which further decomposes to form the primary SnO_2 crystallites. After that, the crystal nuclei of SnO_2 aggregated and grew into SnO_2 nanorods along the c-axis direction, regulated by the morphology controlling agents (NH_4F)[41]. Afterwards, the nanorods self-assemble into the final nanospheres to minimize their large net surface energy as illustrated in Figure 5(a). Furthermore, it has been demonstrated that the SnO_2 morphology could be successfully modulated by Zn doping[34,42,43]. For example, Ding et al.[34] have demonstrated that when the molar ratio of Zn^{2+}/Sn^{4+} exceeds 0.133 in the precursor solution, the morphology of the products can evolve into nanosheets from the nanorod. Thus, Sn^{2+} cations can be substituted when Zn^{2+} cations are introduced into the tin precursor with the same molar ratio (1 : 1), accompanying with the generation of a double ionized oxygen vacancy (V·O). Then, the charge density and the surface energy of each crystal face are changed, indicating the existence of larger polarity in the grown process of Zn-doped SnO_2 nanocrystals[34]. This leads to a different growth rate of the various crystal faces. With the Zn^{2+} ions introduced into the solution, some Sn^{2+} ions are substituted, forming the compound nuclei under the hydrothermal conditions. Then, these nuclei grow into nanosheet structures through aggregation mechanism[44] and Ostwald ripening process[45] under the influence of the Zn^{2+}. Finally, the nanosheets-assemblied nanostructures are formed as shown in Figure 5(b).

The gas sensing properties of SnO_2 and Zn-doped SnO_2 sensors were first measured at different working temperature. Figure 6 exhibits the response of the sensors to 100 ppm glycol, as a function of the operating temperature in a range of 220–360°C. The optimal operating temperature for the sensors is around 240°C and the response is enhanced gradually after the process of calcination and further doped with Zn element. When the temperature is 220°C, the sensors

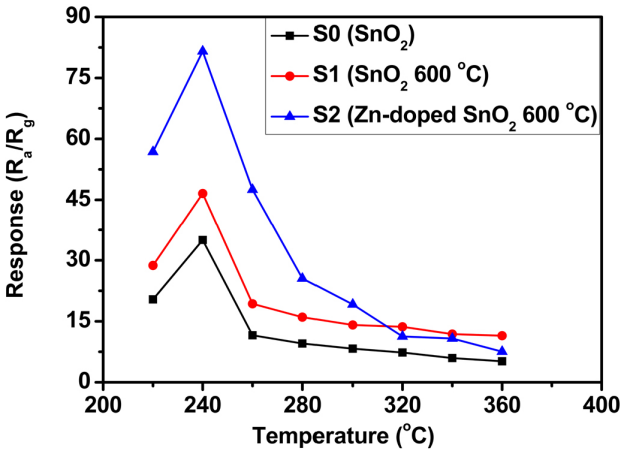

Figure 6 | **The relationship between working temperature and response of three sensors to 100 ppm glycol gas.**

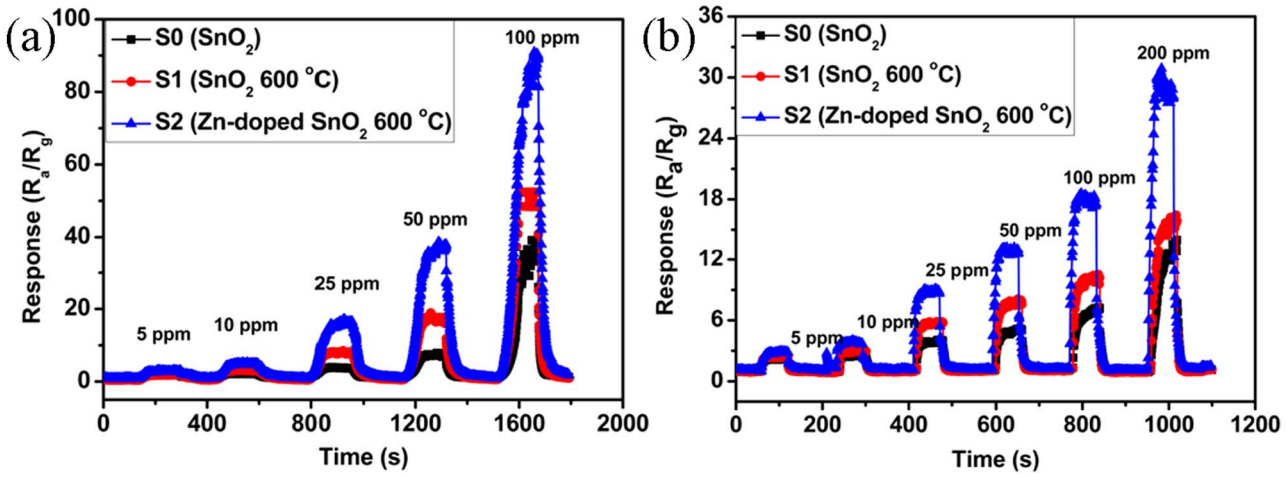

Figure 7 | Response comparisons of three sensors to (a) glycol and (b) ethanol gas of different concentrations at 240°C and 320°C, respectively.

response can reach 50 (Zn-doped SnO_2 sensor) to 100 ppm glycol which is higher than that of others. With the increase of working temperature, the response further increases. Until the temperature is up to 240°C, all the sensors exhibit the maximum response and then decrease as the temperature further increase, which is due to the competing desorption of the chemisorbed oxygen[44,46].

Figure 7(a) shows the response curve of undoped SnO_2 and Zn-doped SnO_2 sensors to glycol of different concentrations from 5 ppm to 100 ppm at 240°C. It can be found that all the sensors responses increase with the increasing concentration of glycol, especially for the Zn-doped SnO_2 sensors. The response increases gradually and can reach to 90 when the glycol concentration is 100 ppm, which is about 2 times higher than that of undoped SnO_2 sensor with calcinations and 3 times higher than that of the sensor without calcinations. It also indicates that the detection limit could be down to 5 ppm-level with a response about 5. Compared with the performance of the sensors to ethanol, as shown in Figure 7(b), glycol gas is more active than ethanol, which leads to a higher response than ethanol. To the best of our knowledge,only Zhang et al.[7] fabricated porous SnO_2 nanotubes sensor to detect glycol while operating at 300°C. Compared with the above, the optimal operating temperature of our sensor is down to 240°C, reduced 60°C than that of porous SnO_2 nanotubes sensor. The further comparison between the sensing performances of our sensor and reported literature is summarized in Table 1.

The response-recovery behavior is also vital characteristic parameters for gas sensors. It was defined as the time needed for the sensor-resistance to change by 90% of the difference from the maximum after injecting and removing the detected gas. It can be clearly observed that the response of Zn-doped SnO_2 sensor increased abruptly after the injection of ethanol and decreased rapidly, then recovered to its initial value after the test gas was released. The response and recovery time are about 14 and 25 s (ethanol), as shown in Figure 8(a). However, when glycol was injected into the box, the response and recovery time was prolonged to 66 s and 97 s (Figure 8(b)), which is much longer than that of ethanol in Figure 8(a). This may be attributed to the lower operating temperature (240°C) and higher boiling point of glycol (197.3°C).

Selective detection of the target gas remains a challenge for the application of metal oxide semiconductor based gas sensor[50]. To identify the selectivity of the three sensors, the cross response properties of the sensors were examined by exposing the sensors to 100 ppm glycol and other gases like ethanol, acetone, benzene, paraxylene,water and hydrogen at 240°C, as summarized in Figure 9. It was seen that the response of Zn-doped SnO_2 sensor to 100 ppm glycol is much higher than that of other sensors. The response can reach to 80, which was about four times higher than the response of ethanol and more than eight times than that of other gases, indicating an excellent selectivity to glycol.

As a typical n-type metal oxide semiconductor, SnO_2 based sensor belongs to the surface-controlled type, and the most widely accepted model is the formation of a charge depletion layer in the near-surface region of each grain, relative to the interior parts, due to electron trapping on adsorbed oxygen species[31,51]. The conductance of the n-type semiconductor is determined by the amount of electrons in its conduction band. Thus, according to a standard model[52], when SnO_2 sensor is exposed to air, oxygen molecules will be adsorbed on its surface and further capture electrons from the conduction band to form oxygen ions (O_2^-, O^{2-}, O^-). It will form a depletion region, resulting in the increase of the sensors resistance. When the sensors are exposed to a reducing gas such as glycol or ethanol, the oxygen negative ions will react with the target gas molecules and release the trapped electrons back to the conduction band of SnO_2, which reduce the amount of surface adsorbed oxygen species, and lead to an increase of the carrier concentrations of the sensors. Consequently, the depletion layer on the surface of the sensors becomes thin, which exhibit the decrease of sensor resistance[7,53]. Based on the formula of response ($S = R_a/R_g$), the sensor shows a high response. Moreover, after the doped of Zn, the response of the sensors is enhanced

Table 1 | Sensing properties of Zn-doped SnO_2 hierarchical nanostructures and other reported gas sensors working under different operating temperatures

Sensing materials (preparation)	[ethanol/glycol](ppm)	R_a/R_g	T_{sens}(°C)
SnO_2–ZnO thin film[47]	200 (ethanol)	4.69	300
Zn-doped SnO_2 nanorods[30]	200 (ethanol)	17	270
ZnO-doped porous SnO_2 nanospheres[48]	200 (ethanol)	20	150
SnO_2/ZnO hierarchical nanostructures[49]	100 (ethanol)	6.2	400
Porous SnO_2 Nanotubes[7]	200 (ethanol) 20 (glycol)	16.7 17.2	300
Our work	200 (ethanol) 100 (glycol)	33 90	320 240

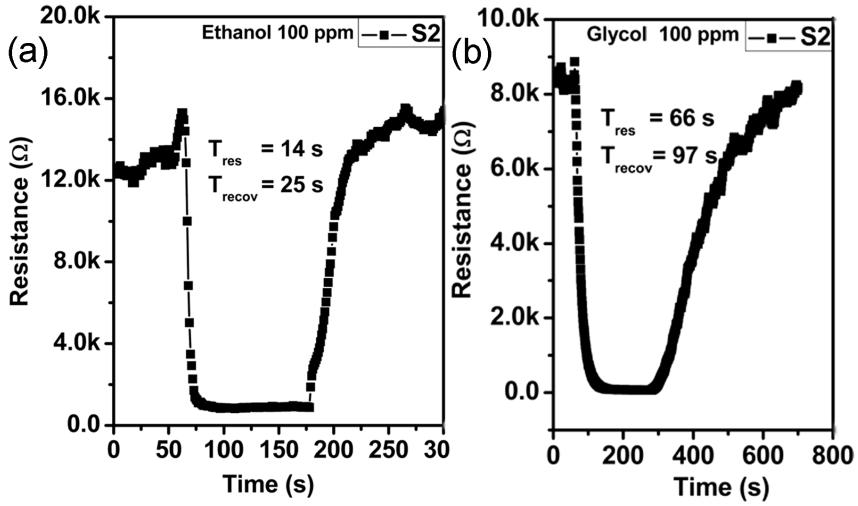

Figure 8 | Response and recovery time of the S2 (Zn-doped SnO_2 600°C) sensor to 100 ppm ethanol and glycol gas at the operating temperature of 320°C and 240°C, respectively.

obviously. The high response of Zn-doped SnO_2 observed here can be attributed to the following factors. Firstly, the grain size of SnO_2 will decrease with the doped of Zn. Due to the above mentioned, the surfaces of the SnO_2 nanosheets become more reactive and absorb more oxygen molecules to form ionized oxygen species[32,54]. Secondly, the specific surface area of Zn-doped SnO_2 is increased. This means that the amount of oxygen can be absorbed and ionized on the surface of Zn-doped SnO_2. In addition, according to the solid state chemistry theory, the quantity of oxygen vacancies in Zn-doped SnO_2 nanostructures is also increased due to the substitution of Zn^{2+} for Sn^{4+}. Thus, owing to the more oxygen species adsorbed on the surface of SnO_2 and more surface oxygen vacancies in the Zn-doped SnO_2 nanostructures, the Zn-doped SnO_2 sensor shows a higher response.

Figure 10(a) shows variations in adsorption spectra of MO organics dye solution in the presence of the Zn-doped SnO_2 (S2) photocatalyst irradiated by a UV lamp for different time. It indicates that the concentration of MO decreases as the irradiation time increasing by measuring the intensity of characteristic absorption peak (465 nm). Different degradation efficiencies for MO, S0, S1 and S2 can be observed directly in Figure 10(b). It can be seen obviously that S2 (Zn-doped SnO_2) exhibits more excellent photocatalytic activity toward MO with the degradation efficiency of 92% than that of others (MO, 23%; S0, 55%; S1, 75%). Moreover, the photocatalytic performance is also much higher than those reported. For example, Yang et al.[55] synthesized ZnO-SnO_2 composite to degrade MO dye, and the degradation efficiency only reached to 60% in 100 min. Kowsari et al.[56] also fabricated ZnO/SnO_2 nanocomposites to degrade MO dye, and the degradation time was longer than 200 min. The higher degradation efficiency may be ascribed to the specific morphology of S2, which provides larger specific surface area than others, as shown in Figure 4. Compared with S0, the degradation efficiency of S1 was enhanced to 75% from 55% (S0), which indicates an increase of photocatalytic activity after the process of calcinations, leading to better crystallinity. Generally, the crystallinity of the photocatalysts plays a crucial role in the enhancement of the separation of the e^-/h^+ pairs.

In general, the specific surface area plays a main role during photocatalytic degradation of dye molecules. On the basis of the photocatalytic mechanism[57–59], it is known that the highly reactive ·OH and O_2^- are generated on the surface of photocatalysis under UV radiation[1]. Therefore, the surface characteristic of nanoparticles will greatly influence its photocatalytic activity. On the basis of the above analysis, the Zn-doped SnO_2 catalyst showed the best photocatalytic activity, this result can be attributed to the special hierarchical structure, and better crystallinity.

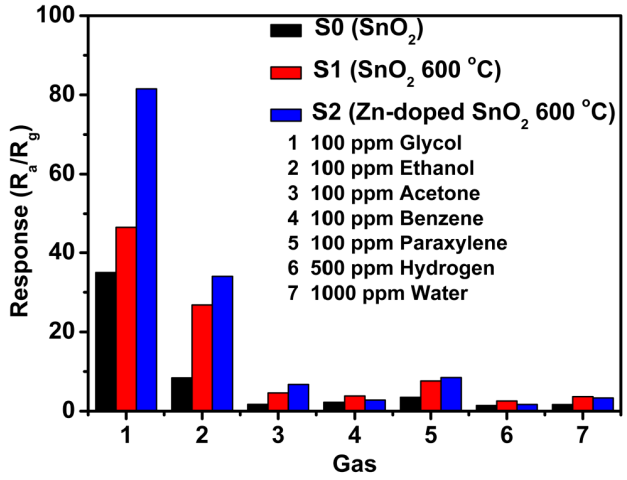

Figure 9 | Selectivity of three sensors for different target gases with same concentration at 240°C.

Conclusion

In summary, a facile and simple method has been developed for preparing undoped and Zn-doped SnO_2 nanostructures. The as-prepared Zn-doped SnO_2 hierarchical architectures were consisted of interconnected ultrathin nanosheets. It was found that the Zn doping plays an important role in controlling the morphologies and structures of the products. The as-prepared nanostructures were used as the efficient gas sensing materials to detect a series of flammable and explosive gases, and photocatalysts for the degradation of methyl orange (MO) under UV irradiation. The Zn-doped SnO_2 gas sensor exhibits highly sensitive and selective sensing properties to glycol gas. The response can reach to 90 for 100 ppm glycol which is much higher than that of undoped SnO_2. The as-prepared Zn-doped SnO_2 hierarchical nanostructures were also used as efficient photocatalyst and exhibited excellent degradation for MO. The photocatalytic MO degradation rate of Zn-doped SnO_2 catalyst is much higher than that of undoped SnO_2 at the same UV irradiation time. This work demonstrates that the simply prepared Zn-doped SnO_2

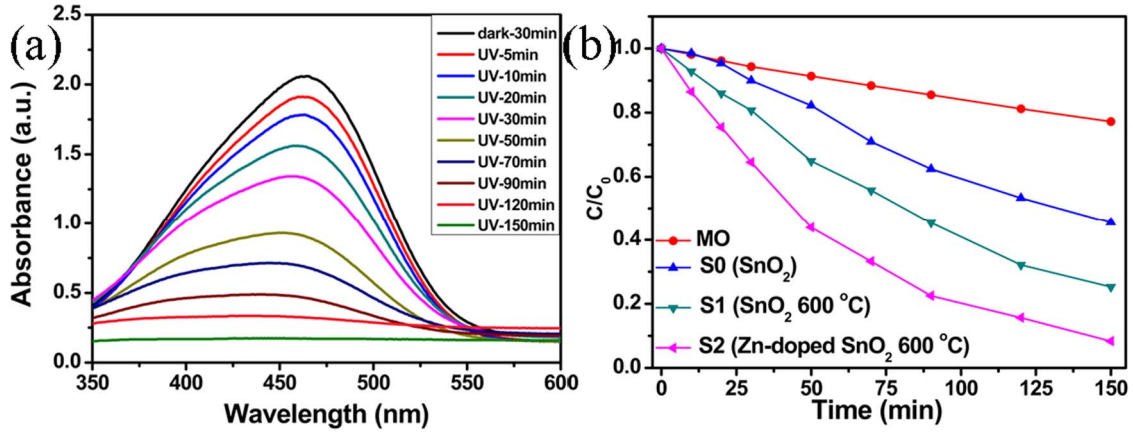

Figure 10 | Variations in adsorption spectra of MO organics dye solution in the presence of the photocatalyst irradiated by a UV lamp for different time: (a) S2 (Zn-doped SnO_2 600°C), and (b) photocatalytic degradation of MO, S0, S1, S2.

nanostructures have a potential application in glycol gas sensor or MO photocatalystic degradation.

1. Liu, Y. *et al.* Hierarchical SnO_2 nanostructures made of intermingled ultrathin nanosheets for environmental remediation, smart gas sensor, and supercapacitor applications. *ACS Appl. Mater. Interfaces* **6**, 2174–2184 (2014).
2. Wang, H. K. *et al.* Engineering of facets, band structure, and gas-sensing properties of hierarchical Sn^{2+}-doped SnO_2 nanostructures. *Adv. Funct. Mater* **23**, 4847–4853 (2013).
3. Zhang, D. F., Sun, L. D., Yin, J. L. & Yan, C. H. Low-temperature fabrication of highly crystalline SnO_2 nanorods. *Adv. Mater* **15**, 1022–1025 (2003).
4. Hou, X. J. *et al.* SnO_2-microtube-assembled cloth for fully flexible self-powered photodetector nanosystems. *Nanoscale* **5**, 7831–7837 (2013).
5. Wang, L. *et al.* Synthesis of hierarchical SnO_2 nanostructures assembled with nanosheets and their improved gas sensing properties, *Sensor Actuat. B-Chem* **188**, 85–93 (2013).
6. Ju, D. X., Xu, H. Y., Zhang, J., Guo, J. & Cao, B. Q. Direct hydrothermal growth of ZnO nanosheets on electrode for ethanol sensing. *Sensor Actuat. B-Chem* **201**, 444–451 (2014).
7. Zhang, J., Guo, J., Xu, H. Y. & Cao, B. Q. Reactive-template fabrication of porous SnO_2 nanotubes and their remarkable gas-sensing performance. *ACS Appl. Mater. Interfaces* **5**, 7893–7898 (2013).
8. Dai, P. *et al.* Two-solvent method synthesis of SnO_2 nanoparticles embedded in SBA-15: gas-sensing and photocatalytic properties study. *Mater. Res. Bull* **50**, 440–445 (2014).
9. Kim, H. R. *et al.* The role of NiO doping in reducing the impact of humidity on the performance of SnO_2-based gas sensors: synthesis strategies, and phenomenological and spectroscopic studies. *Adv. Funct. Mater* **21**, 4456–4463 (2011).
10. Yang, R., Zhao, W., Zheng, J., Zhang, X. Z. & Li, X. G. One-step synthesis of carbon-coated tin dioxide nanoparticles for high lithium storage. *J. Phys. Chem. C* **114**, 20272–20276 (2010).
11. Yang, R., Gu, Y. G., Lia, Y. Q., Zheng, J. & Lia, X. G. Self-assembled 3D flower-shaped SnO_2 nanostructures with improved electrochemical performance for lithium storage. *Acta Mater* **58**, 866–874 (2010).
12. Xu, X. J. *et al.* Structural transformation, photocatalytic, and field-emission properties of ridged TiO_2 nanotubes. *ACS Appl. Mater. Interfaces* **3**, 1352–1358 (2011).
13. Dai, Z. R., Gole, J. L., Stout, J. D. & Wang, Z. L. Tin oxide nanowires, nanoribbons, and nanotubes. *J. Phys. Chem. B* **106**, 1274–1279 (2002).
14. Zheng, L. *et al.* Photocatalytic activity of $ZnO/Sn_{1-x}Zn_xO_{2-x}$ nanocatalysts: a synergistic effect of doping and heterojunction. *Appl. Catal. B: Environ* **148–149**, 44–50 (2014).
15. Zhang, S. *et al.* Controllable synthesis of recyclable core-shell γ-Fe_2O_3@SnO_2 hollow nanoparticles with enhanced photocatalytic and gas sensing properties. *Phys. Chem. Chem. Phys* **15**, 8228–8236 (2013).
16. Talebian, N. & Jafarinezhad, F. Morphology-controlled synthesis of SnO_2 nanostructures using hydrothermal method and their photocatalytic applications. *Ceram. Int* **39**, 8311–8317 (2013).
17. Han, Y. T. *et al.* Solution growth and cathodoluminescence of novel SnO_2 core-Shell homogeneous microspheres. *J. Phys. Chem. C* **114**, 8235–8240 (2010).
18. Guo, J., Zhang, J., Ju, D. X., Xu, H. Y. & Cao, B. Q. Three-dimensional SnO_2 microstructures assembled by porous nanosheets and their superior performance for gas sensing. *Powder Technol* **250**, 40–45 (2013).
19. Dai, S. & Yao, Z. Synthesis of flower-like SnO_2 single crystals and its enhanced photocatalytic activity. *Appl. Surf. Sci* **258**, 5703–5706 (2012).
20. Wang, W. C. *et al.* Enhanced ethanol sensing properties of Zn-doped SnO_2 porous hollow microspheres. *Appl. Surf. Sci* **261**, 890–895 (2012).
21. Cui, S. M. *et al.* Indium-doped SnO_2 nanoparticle-graphene nanohybrids: simple one-pot synthesis and their selective detection of NO_2. *J. Mater. Chem. A* **1**, 4462–4467 (2013).
22. Mondal, B. *et al.* ZnO-SnO_2 based composite type gas sensor for selective hydrogen sensing. *Sensor Actuat. B-Chem* **194**, 389–396 (2014).
23. Tang, W., Wang, J., Yao, P. & Li, X. Hollow hierarchical SnO_2-ZnO composite nanofibers with heterostructure based on electrospinning method for detecting methanol. *Sensor Actuat. B-Chem* **192**, 543–549 (2014).
24. Zhang, J., Liu, X., Wu, S., Xu, H. & Cao, B. Q. One-pot fabrication of uniform polypyrrole/Au nanocomposites and investigation for gas sensing. *Sensor Actuat. B-Chem* **186**, 695–700 (2013).
25. Zhang, J. *et al.* Au-functionalized hematite hybrid nanospindles: general synthesis, gas sensing and catalytic properties. *J. Phys. Chem. C* **115**, 5352–5357 (2011).
26. Guo, J. *et al.* High-performance gas sensor based on ZnO nanowires functionalized by Au nanoparticles. *Sensor Actuat. B-Chem* **199**, 339–345 (2014).
27. Ju, D. X. *et al.* Highly sensitive and selective triethylamine-sensing properties of nanosheets directly grown on ceramic tube by forming NiO/ZnO PN heterojunction. *Sensor Actuat. B-Chem* **200**, 288–296 (2014).
28. Wang, X., Fan, H. & Ren, P. Self-assemble flower-like SnO_2/Ag heterostructures: correlation among composition, structure and photocatalytic activity. *Colloid. Surface. A* **419**,140–146 (2013).
29. Jia, T. *et al.* Synthesis, characterization, and photocatalytic activity of Zn-Doped SnO_2 hierarchical architectures assembled by nanocones. *J. Phys. Chem. C* **113**, 9071–9077 (2009).
30. Huang, H. *et al.* Needle-like Zn-doped SnO_2 nanorods with enhanced photocatalytic and gas sensing properties. *Nanotechnology* **23**, 105502 (2012).
31. Guan, Y. *et al.* Hydrothermal preparation and gas sensing properties of Zn-doped SnO_2 hierarchical architectures. *Sensor Actuat. B-Chem* **191**, 45–52 (2014).
32. Li, Z., Zhou, Y., Yu, T., Liu, J. & Zou, Z. Unique Zn-doped SnO_2 nano-echinus with excellent electron transport and light harvesting properties as photoanode materials for high performance dyesensitized solar cell. *CrystEngComm* **14**, 6462–6468 (2012).
33. Ahn, H. J., Choi, H. C., Park, K. W., Kim, S. B. & Sung, Y. E. Investigation of the structural and electrochemical properties of size-controlled SnO_2 nanoparticles. *J. Phys. Chem. B* **108**, 9815–9820 (2004).
34. Ding, X., Zeng, D. & Xie, C. Controlled growth of SnO_2 nanorods clusters via Zn doping and its influence on gas-sensing properties. *Sensor Actuat. B-Chem* **149**, 336–344 (2010).
35. Mathew, X. *et al.* Structural modifications of SnO_2 due to the incorporation of Fe into the lattice. *J. Appl. Phys* **100**, 073907 (2006).
36. Jia, T. *et al.* Facile synthesis of Zn-doped SnO_2 dendrite-built hierarchical cube-like architectures and their application in lithium storage, *Mater. Sci. Eng. B* **189**, 32–37 (2014).
37. Liu, X., Iqbal, J., Wu, Z., He, B. & Yu, R. Structure and room-temperature ferromagnetism of Zn-doped SnO_2 nanorods prepared by solvothermal method. *J. Phys. Chem. C* **114**, 4790–4796 (2010).
38. Shek, C. H., Lin, G. M. & Lai, J. K. L. Effect of oxygen deficiency on the Raman spectra and hyperfine interactions of nanometer SnO_2, *Nanostruct. Mater* **11**, 831 (1999).
39. Cheng, G. *et al.* Solvothermal controlled growth of Zn-doped SnO_2 branched nanorod clusters. *Cryst. Growth* **309**, 53–59 (2007).
40. Zeng, Y. *et al.* Development of microstructure CO sensor based on hierarchically porous ZnO nanosheet thin films. *Sensor Actuat. B-Chem* 173, 897–902 (2012).
41. Wang, H. Hydrothermal synthesis of hierarchical SnO_2 microspheres for gas sensing and lithium-ion batteries applications: Fluoride-mediated Formation of Solid and Hollow Structures. *J. Mater. Chem* **22**, 2140–2148 (2012).

42. Li, Z., Li, X., Zhang, X. & Qian, Y. Hydrothermal synthesis and characterization of novel flower-like zinc-doped SnO_2 nanocrystals, *J. Cryst. Growth* **291**, 258–261 (2006).
43. Cheng, G., Wu, K., Zhao, P., Cheng, Y., He, X. & Huang, K. Solvothermal controlled growth of Zn-doped SnO_2 branched nanorod clusters, *J. Cryst. Growth* **309**, 53–59 (2007).
44. Leite, E. R., Giraldi, T. R., Pontes, F. M. & Longo, E. Crystal growth in colloidal tin oxide nanocrystals induced by coalescence at room temperature, *Appl. Phys. Lett* **83**, 1566–1568 (2003).
45. Liu, Z. P. *et al.* Complex-surfactant-assisted hydrothermal route to ferromagnetic nickel nanobelts, *Adv. Mater* **15**, 1946–1948 (2003).
46. Bie, L. J. *et al.* Nanopillar ZnO gas sensor for hydrogen and ethanol, *Sensor Actuat. B-Chem* **126**, 604–608 (2007).
47. Kim, K.-W. *et al.* The selective detection of C_2H_5OH using SnO_2-ZnO thin film gas sensors prepared by combinatorial solution deposition, *Sensor Actuat. B-Chem* **123**, 318–324 (2007).
48. Ma, X., Song, H. & Guan, C. Enhanced ethanol sensing properties of ZnO-doped porous SnO_2 hollow nanospheres, *Sensor Actuat. B-Chem* **188**, 193–199 (2013).
49. Khoang, N. D., Trung, D. D., Duy, N. V., Hoa, N. D. & Hieu, N. V. Design of SnO_2/ZnO hierarchical nanostructures for enhanced ethanol gas-sensing performance, *Sensor Actuat. B-Chem* **174**, 594–601 (2012).
50. Chiu, H. C. & Yeh, C. S. Hydrothermal synthesis of SnO_2 nanoparticles and their gas-sensing of alcohol. *J. Phys. Chem. C* **111**, 7256–7259 (2007).
51. Thong, L. V. *et al.* On-chip fabrication of SnO_2-nanowire gas sensor: The effect of growth time on sensor performance. *Sensor Actuat. B-Chem* **146**, 361–367 (2010).
52. Barsan, N. & Weimar, U. Conduction model of metal oxide gas sensors. *J. Electroceram* **7**, 143–167 (2001).
53. Xu, J. Q., Chen, Y. P., Chen, D. Y. & Shen, J. N. Hydrothermal synthesis and gas sensing characters of ZnO nanorods. *Sensor Actuat. B-Chem* **113**, 526–531 (2006).
54. Xu, C. N., Tamaki, J., Miura, N. & Yamazoe, N. Grain size effects on gas sensitivity of porous SnO_2-based elements. *Sensor Actuat. B-Chem* **3**, 147–155 (1991).
55. Yang, Z., Lv, L., Dai, Y., Xu, Z. & Qian, D. Synthesis of ZnO-SnO_2 composite oxides by CTAB-assisted co-precipitation and photocatalytic properties, *Appl. Surf. Sci* **256**, 2898–2902 (2010).
56. Kowsari, E. & Ghezelbash, M. R. Ionic liquid-assisted, facile synthesis of ZnO/SnO_2 nanocomposites, and investigation of their photocatalytic activity, *Mater. Lett* **68**, 17–20 (2012).
57. Ohko, Y., Fujishima, A. & Hashimoto, K. Kinetic analysis of the photocatalytic degradation of gas-phase 2-propanol under mass transport-limited conditions with a TiO_2 film photocatalyst. *J. Phys. Chem. B* **102**, 1724–1729 (1998).
58. Song, X. F. & Gao, L. Fabrication of hollow hybrid microspheres coated with silica/titania via sol-gel process and enhanced photocatalytic activities. *J. Phys. Chem. C* **111**, 8180–8187 (2007).
59. Wang, X., Fan, H. & Ren, P. UV Light-assisted synthesis of coral SnO_2: characterization and its enhanced photocatalytic properties. *Colloid. Surfaces A* **402**, 53–59 (2012).

Acknowledgments

Thanks University of Jinan (UJn) for the support on new staff, and the project supported by the Taishan Scholar (No. TSHW20120210), the National Natural Science Foundation of China (Grant No. 11304120, 11174112, 61106059), the Encouragement Foundation for Excellent Middle-aged and Young Scientist of Shandong Province (Grant No. BS2012CL005).

Author contributions

Z.Q.Q. and J.D.X. designed the experiments. Z.Q.Q. performed the experiments. H.J.Z. and D.X.L. performed the SEM observations. C.B.Q. performed TEM observations. Z.Q.Q., J.D.X. and X.X.J. discussed and commented on the experiments and results, and wrote the paper.

Additional information

Competing financial interests: The authors declare no competing financial interests.

How to cite this article: Zhao, Q. *et al.* Morphology-modulation of SnO_2 Hierarchical Architectures by Zn Doping for Glycol Gas Sensing and Photocatalytic Applications. *Sci. Rep.* **5**, 7874; DOI:10.1038/srep07874 (2015).